Materials Today Bio 20 (2023) 100683

Contents lists available at ScienceDirect

Materials Today Bio

journal homepage: www.journals.elsevier.com/materials-today-bio

Fabrication of a composite 3D-printed titanium alloy combined with controlled in situ drug release to prevent osteosarcoma recurrence

Daoyang Fan [a,b,1], Chaoqi Zhang [c,1], Hufei Wang [d,e], Qingguang Wei [a], Hong Cai [a], Feng Wei [a], Zhilei Bian [f], Weifeng Liu [b,***], Xing Wang [d,e,**], Zhongjun Liu [a,*]

[a] Department of Orthopedics, Peking University Third Hospital, Beijing, 100191, China
[b] Department of Orthopaedic Oncology Surgery, Beijing Jishuitan Hospital, Peking University, Beijing, 100035, China
[c] Department of Thoracic Surgery, National Cancer Center/National Clinical Research Center for Cancer/Cancer Hospital, Chinese Academy of Medical Sciences and Peking Union Medical College, Beijing, 100021, China
[d] Beijing National Laboratory for Molecular Sciences, Institute of Chemistry, Chinese Academy of Sciences, Beijing, 100190, China
[e] University of Chinese Academy of Sciences, Beijing, 100049, China
[f] Department of Hematology, First Affiliated Hospital of Zhengzhou University, Zhengzhou, 450000, China

ARTICLE INFO

Keywords:
3D-printed titanium
Osteosarcoma recurrence
Prodrug
Local delivery
pH-responsive

ABSTRACT

Osteosarcoma is a malignant bone tumor occurring in adolescents. Surgery combined with adjuvant or neoadjuvant chemotherapy is the standard treatment. However, systemic chemotherapy is associated with serious side effects and a high risk of postoperative tumor recurrence, leading to a high amputation rate and mortality in cancer patients. Implant materials that can simultaneously repair large bone defects and prevent osteosarcoma recurrence are in urgent need. Herein, an intelligent system comprising 3D-printed titanium scaffold (TS) and pH-responsive PEGylated paclitaxel prodrugs was fabricated for bone defect reconstruction and recurrence prevention following osteosarcoma surgery. The drug-loaded implants exhibited excellent stability and biocompatibility for supporting the activity of bone stem cells under normal body fluid conditions and the rapid release of drugs in response to faintly acidic environments. An *in vitro* study demonstrated that five human osteosarcoma cell lines could be efficiently eradicated by paclitaxel released in an acidic microenvironment. Using mice models, we demonstrated that the drug-loaded TS can enable a pH-responsive treatment of postoperative tumors and effectively prevent osteosarcoma recurrence. Therefore, local implantation of this composite scaffold may be a promising topical therapeutic method to prevent osteosarcoma recurrence.

1. Introduction

Osteosarcoma is the most common primary bone malignant tumor, typically occurring in adolescents or in children under the age of 20; it is highly malignant [1]. The annual incidence rate is approximately 5/1,000,000, resulting in approximately 50,000 new cases each year worldwide [2]. The total five-year survival rate of osteosarcoma patients is in the range of 60%–80% [3]. The conventional treatment is preoperative chemotherapy, followed by surgical treatment and postoperative chemotherapy [1]. Generally, incomplete or residual tumor resection after surgical resection is the main reason for postoperative recurrence and metastasis because the microenvironment following tumor resection may promote tumor growth and metastasis. Other existing clinical programs, such as long-term intravenous and systemic chemotherapy, are often associated with serious side effects (e.g., gastrointestinal intolerance, neutropenia, cardiotoxicity, nephrotoxicity, and neurotoxicity) as well as a high amputation rate [1,2]. Even with proper surgery resection, the local recurrence rate of osteosarcoma remains in the range of 15%–30% [4], and the five-year survival rate after local recurrence is significantly reduced [5]. This has led to a dilemma in terms of the clinical treatment at this stage. Large bone defect repair after tumor resection and in situ control of osteosarcoma recurrence are the two main issues requiring urgent solutions.

After the surgical removal of osteosarcoma lesions, bone defect

* Corresponding author. Department of Orthopedics, Peking University Third Hospital, Beijing, 100191, China.
** Corresponding author. Beijing National Laboratory for Molecular Sciences, Institute of Chemistry, Chinese Academy of Sciences, Beijing, 100190, China.
*** Corresponding author. Department of Orthopaedic Oncology Surgery, Beijing Jishuitan Hospital, Peking University, Beijing, 100035, China.
E-mail addresses: liuweifeng@jst-hosp.com.cn (W. Liu), wangxing@iccas.ac.cn (X. Wang), zjliu@bjmu.edu.cn (Z. Liu).
[1] These authors contributed equally to the work.

https://doi.org/10.1016/j.mtbio.2023.100683
Received 12 February 2023; Received in revised form 28 April 2023; Accepted 23 May 2023
Available online 24 May 2023

reconstruction must be performed to ensure the transmission of skeletal muscle strength. Three-dimensional printed implants have been widely used in clinical treatment, including vascular stents, fracture prostheses, and tumor resection supports [6–9]. Among metal implants, prosthesis made of 3D-printed titanium alloys has been proven safe after years of clinical application and experimental research [10]. Several studies have shown that the material used in this study has excellent mechanical support, good biological safety, and physical-chemical properties [6, 10–13]. With the advantages of individualized adaptation and osteogenesis, 3D-printed porous alloys are becoming irreplaceable in the clinical treatment of bone tumors.

In most cases, tumor recurrence stems from an incomplete surgical resection of the original site. The remaining tumor cells regrow in the body, resulting in tumor recurrence in situ [14,15]. Methods that can help avoid this phenomenon have been a topic of related research. In the clinical treatment of osteosarcoma, postoperative chemotherapies are widely applied in patients with tumor resection. Paclitaxel (PTX) is an effective drug for treating chemo-sensitive tumors [16,17]. However, after the systemic application of chemotherapy drugs, side effects, including weight loss, anorexia, diarrhea, and bone marrow suppression, are inevitable [16,18]. Patients may die from these side effects rather than the tumor recurrence. To solve this problem, targeted nanoparticles (NPs) with a suitable size range (10–250 nm) are an ideal choice because they can uptake and retain their function at the tumor site via enhanced permeability and retention (EPR) [19]. The advantages of a localized drug-delivery system lie in the direct delivery of high-concentration drugs to the tumor sites, thereby improving the medication effect and reducing the systemic side effects. Based on this advantage, many advanced environmentally responsive NPs have been designed and developed, such as polymeric NPs, micelles, vesicles, nanogels, and liposomes [20–22]. Among them, prodrug-based NPs have received much attention owing to their simple structure and potential in clinical translation [23–25]. In the case of many malignant tumors, an acidic environment is present locally in the microenvironment because of glycolysis and lactic acid accumulation in the tumor [26,27]. This acidic environment has been considered as an efficient trigger for drug release, and prodrugs conjugated with a pH-responsive linker can be triggered in the acidic environment of intracellular endosomal/lysosomal compartments [28,29].

If a titanium alloy prosthesis can be imparted with an antitumor function by surface loading with chemotherapeutic drugs, it may be beneficial in reducing the local in situ recurrence rate following osteosarcoma surgery. With the drug-carrying system of PTX on the surface of a titanium alloy, a 3D-printed porous titanium alloy implant with a high antitumor efficiency and controllable release system is urgently required to prevent the local recurrence of osteosarcoma following surgery.

Hence, inspired by the clinical treatment of chemo-sensitive bone tumors and corresponding drug delivery systems, in this study, we developed a localized drug-delivery system with pH-responsive anticancer prodrugs loaded onto a 3D-printed titanium scaffold (TS), to prevent osteosarcoma recurrence. As illustrated in Fig. 1, an amphiphilic polymer prodrug of poly (ethylene glycol)–acetal–paclitaxel (PEG–acetal–PTX), denoted by PAP, is facilely prepared via simple chemical reactions. As illustrated in a previous work [30], PAP can self-assemble into the acid-labile micellar NPs in an aqueous medium, thereby improving the solubility of the PTX drug and promoting the plasma residence time. Therefore, PAP NPs could be used as a novel delivery system with a rapid acid response and large drug-loading capacity. After anchoring onto the surface of the 3D-printed TS implant via polydopamine (PDA), the TS@PAP composite scaffold was constructed with simultaneous strength support for bone growth and pH-responsive drug-release capability for tumor therapy. After implantation at the surgical site, TS@PAP can potentially rapidly respond to the tumor microenvironment, triggering drug release and effectively preventing

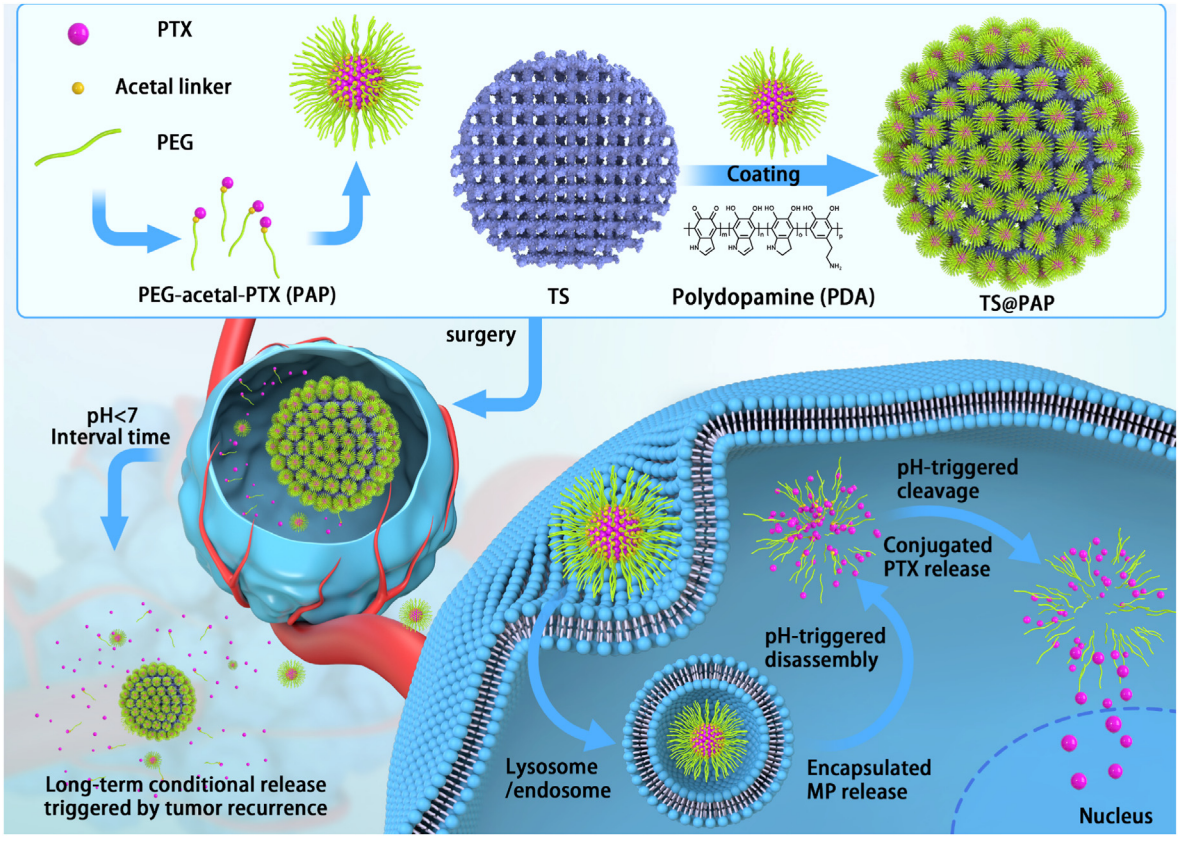

Fig. 1. Schematic of the formation of a TS@PAP composite scaffold for tumor therapy and prevention of osteosarcoma recurrence.

osteosarcoma recurrence. Thus, this delivery system may be developed as an ideal therapeutic regimen to control the local tumor residual and postoperative the tumor regeneration, while promoting the repair of large bone defects without increasing the patient's treatment burden or causing excessive contraction. Overall, this study illustrated a novel and reliable tumor recurrence surveillance strategy based on the pH changes in the tumor microenvironment, demonstrating effective control of local tumor recurrence within a tumor recurrence animal model.

2. Results and discussion

2.1. Synthesis of PEG–acetal–PTX prodrug

The acetal-linked PEGylated PTX prodrug PAP was synthesized following the synthetic route shown in Fig. 2A. After efficient anhydride and esterification reactions, a PEG–vinyl ether derivative was obtained by the reaction with PTX, yielding the targeted PAP in the presence of pyridinium *p*-toluenesulfonate (PPTS). Precise attributes and integration

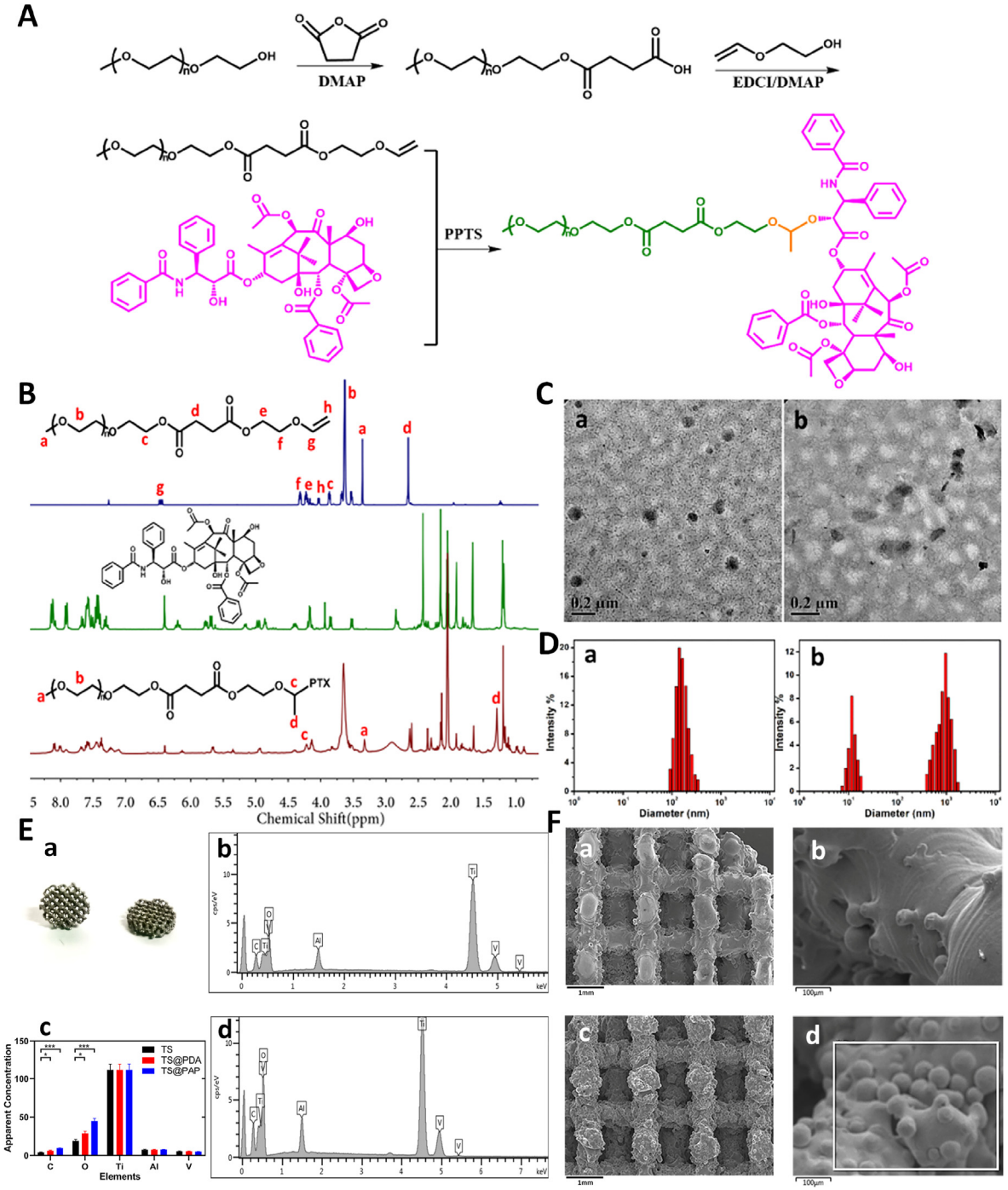

Fig. 2. (A) Synthesis route for the PEG–acetal–PTX prodrug. (B) ^{1}H NMR spectra of PEG–vinyl ether, PTX, and PEG–acetal–PTX. (C) TEM images and (D) size distribution of PAP NPs under pH values of (a) 7.4 and (b) 6.5. (E) General appearance and energy spectra analysis of the 3D-printed prosthesis. (a) General appearance; (c) Quantitative elemental analysis ($n = 5$, $^{*}P < 0.05$, $^{***}P < 0.01$). (b, d) Energy spectra analysis of the surface elements. (F) SEM images of TS (a and b, scale bar: 1 mm) and TS@PAP (c and d, scale bar: 100 μm).

peak ratios of the ether-linked PEG derivative could be clearly seen in the upper panel of Fig. 2B, demonstrating its successful synthesis. In addition, the new peaks emerging at $\delta = 4.0–4.5$ and 1.0–1.5 ppm in the ^{1}H NMR spectrum shown in the bottom panel of Fig. 2B could be attributed to the acetal group, and the disappeared peaks at δ = 5.5–6.5 ppm indicated the successful conjugation of the targeted PAP with an explicit chemical structure. The PTX content in the PAP prodrug was calculated to be 48.1%, which is higher than those of most reported PTX prodrugs [31,32].

2.2. Preparation, stability, and pH-responsive destabilization of PAP NPs

In aqueous solutions, the amphiphilic PAP polymer can self-assemble into micelles. The transmission electron microscopy (TEM) image (Fig. 2C–a) shows spherical structures with a size of ca. 110 nm, and the dynamic light scattering (DLS) result (Fig. 2D–a) shows an average particle size of ca. 185 nm. This size difference is attributed to the swelling state of PAP in an aqueous solution compared with the dry state, as shown in the TEM image. Science the diameter is less than 200 nm, the PAP NPs were suitable to maintain reduced reticule-endothelial system (RES) uptake levels and minimal renal excretion, indicating their potential application as a smart carrier to enhance the passive tumor-targeting capacity via the EPR effect.

On account of the stable linkages between the hydrophobic PTX and hydrophilic PEG under mild conditions, the PAP NPs maintained a satisfactory storage stability for drug formulations. To ensure effective intracellular drug release, it is important for stimuli-responsive prodrugs to meet the requirements of precise targeting and controllable release within the target cells upon changes in the physical and chemical environments therein. The acid-labile acetal group between the hydrophobic PTX and the hydrophilic PEG made the NPs breakable under weakly acidic conditions. After incubating for 2 h in a solution with a pH of 6.5, small blocks and large aggregates could be detected, as shown in Fig. 2C–b and 2D-b, suggesting a pH-induced cleavage of the acetal linkers and degradation of the polymeric NPs. These results demonstrated that the PAP NPs can maintain colloidal stability under extracellular conditions and dissociate rapidly under pH-stimuli that mimic intracellular conditions.

2.3. Characterization of TS@PAP composite scaffolds

The PAP prodrug was facilely anchored onto the surface of the TS with the help of PDA [33,34]. Dopamine can undergo auto-oxidative polymerization under alkaline aerobic conditions, forming an adhesive continuous PDA coating on the surface of the scaffold (TS@PDA). Therefore, the PAP NPs could be co-loaded onto the TS surface to form a TS@PAP composite scaffold. The attachment of spherical NPs can be clearly seen under the scanning electron microscopy (SEM) images. The energy dispersive spectroscopy (EDS) results revealed a significant increase in the C and O contents, indicating the successful coating of the organic compounds or polymeric prodrugs onto the TS scaffolds (Fig. 2E and F).

2.4. In vitro drug release from the TS@PAP scaffold

With a quantitative detection performed using high-performance liquid chromatography (HPLC), the *in vitro* drug release profile of the TS@PAP composite scaffold was assessed under physiological phosphate buffer solution (PBS, pH of 7.4) and acidic conditions (PBS, pH of 6.5) to simulate an endo-lysosomal environment at a temperature of 37 °C. As depicted in Fig. 3A, a negligible amount of PTX is released from the TS@PAP composite scaffold into the solution with a pH of 7.4 at a cumulative release rate of 11.28 ± 0.47% at 72 h. In comparison, a much faster release of PTX is observed in the solution with a pH of 6.5, at a high release rate of 85.33 ± 0.66%; this is attributed to the cleavage of the acetal bonds and accelerated release of PTX. The loading capacity of PTX in the TS@PAP composite scaffold was tested by HPLC treated with mixture of 1 N HCl and acetonitrile (v/v = 1/1). The PTX loading content per TS were 173.82 ± 8.34 μg, which met the drug concentration requirements. This pH change from an extracellular environment (pH of 7.4) to endosomal compartments (pH of 6.5) suggested that the PAP NPs would remain stable and avoid any premature burst release into the

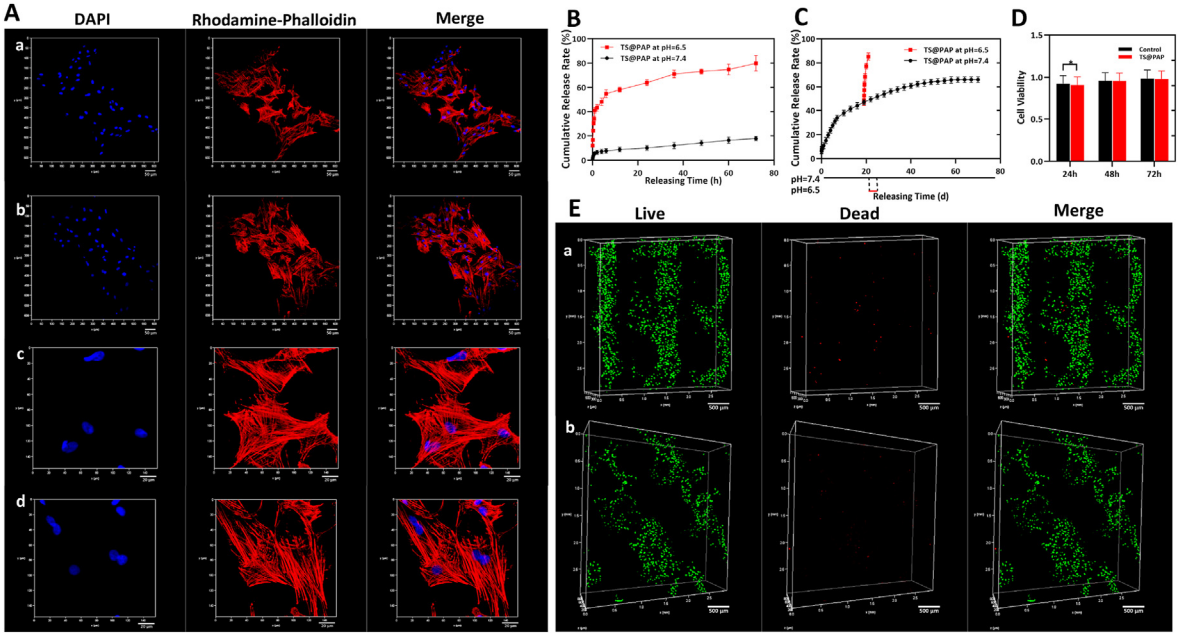

Fig. 3. (A) Double staining of cytoskeleton and nucleus of mBMSC after co-cultivation with TS and TS@PAP implants for 48 h. Confocal microscopy images for TS at 10x (a, scale bar: 50 μm) and 40x (c, scale bar: 20 μm) magnification and for TS@PAP at 10x (b, scale bar: 50 μm) and 40x (d, scale bar: 20 μm) magnification. (B) *In vitro* short-term PTX release in solutions with pH values of 7.4 and 6.5. (C) *In vitro* long-term release of free PTX from TS@PAP implants after incubation at a pH of 6.5. (D) Cell activity of co-cultured mBMSC with TS and TS@PAP implants ($n = 5$, $^*P < 0.05$). (E) Confocal microscopy images of live-dead staining of mBMSC after co-cultivation with TS (a, scale bar: 500 μm) and TS@PAP (b, scale bar: 500 μm) implants for 48 h.

blood stream, while effectively promoting the release of PTX from its prodrug during intracellular trafficking. The sustained release of PTX at a pH of 7.4 could last for more than 1 month; however, upon exposure to an acidic environment, the drug carriers could quickly respond to accelerate the drug release, as shown in Fig. 3B and C. This indicates their potential role in effectively killing tumors in the initial period and continuously exerting a pH-sensitive effect to prevent tumor recurrence over a longer period. Unlike the conventional liposomal PTX, which is associated with poor stability and premature burst release, pH-responsive NPs exhibit a high drug-loading capacity, favorable stability, passive targeting, and tailored PTX release behavior when required, thus significantly promoting tumor endocytosis and enhancing the therapeutic effect.

2.5. *In vitro* cytotoxicity and antitumor efficiency of TS@PAP scaffold

Fig. 3D shows a comparison of the cell viability of the TS@PAP and blank TS groups at 24, 48, and 72 h. After co-cultivation with mouse bone marrow mesenchymal stem cells (mBMSC) for 24 h, the cell activity of the TS@PAP group became slightly lower than that of the TS group, with statistical significance ($P < 0.05$). However, when the incubation time was extended to 48 and 72 h, there was no statistically significant difference in the cell activity between the two groups. Titanium alloy (Ti6Al4V) has been used as an orthopedic implant in clinical applications for many years. For PDA coatings, there have been many related research reports proving their biosafety [35–37]. Therefore, the PAP NPs fully determined the *in vitro* cytotoxicity. To the best of our knowledge, the direct release of PTX into a body fluid environment has a negative impact on the healing of local normal tissues; PEGylated paclitaxel prodrugs exhibited a good stability in the solution with a pH of 7.4 and did not have a significantly negative impact on the mBMSC activity or tissue growth. In addition, previous studies have shown that the release of trace amounts of PTX in normal environments would not significantly affect normal cell formation or healing after local surgical trauma [38,39].

Cell live/dead staining is a green fluorescent labeling technique using Calcein-AM as a dye to identify the death/live status of cells [40]. After co-cultivation with TS and TS@PAP scaffolds for 48 h, most of the cells could crawl along the 3D-printed implant pillars to form a 3D solid adhesive morphology. Fig. 3E–a and b show that most of the cells were stained with green fluorescence, and very few dead cells were stained with PI in red, verifying that the cells could effectively survive on the surface of drug-loaded implants under normal conditions. Compared with the TS group, the cells in the TS@PAP group also maintained a good survival status. In particular, there were fewer dead cells stained with propidium iodide than in the TS group in some areas. There was no statistical difference in the fluorescence intensity quantification between the two groups. However, a simple cell live/dead staining cannot precisely reflect the entire situation, because cells may appear to be stained with Calcein-AM but their activity may not be ideal. Therefore, to determine the survival status of the cells and observe the microscopic morphology on the TS and TS@PAP scaffolds, the cytoskeleton was stained with rhodamine-phalloidin-labeled F-actin, and the nucleus was stained blue using 4′,6-diamidino-2-phenylindole (DAPI). Paclitaxel affects cell mitosis, causing intracellular denaturation of F-actin protein and apoptosis [41]. Fig. 3A–a and b showed that the nucleus was well distributed in the mBMSC without any of the following observations: multiple nuclei, nuclear shrinkage, cytoskeletal defect, or cytoskeleton fragmentation. This further proved the negligible escape of PTX from the scaffolds and good biosafety of the TS@PAP composite scaffold in terms of cell and tissue growths under normal conditions. Fig. S1 showed the cell images of the co-cultured osteosarcoma cells with 3D-printed titanium alloy implants in different pH culture media. With a high PAP loading solution for TS@PAP composite scaffolds, the cell viability of BMSCs would be significantly affected. While osteosarcoma cells (143 B) could not be efficiently killed with low PAP loading solutions. To effectively balance the ability of the TS@PAP scaffold to kill tumor cells without unduly affecting normal tissue healing, a PAP concentration of 5 mmol/L was thus chosen in the study (Fig. S2). The osteogenesis and osseointegration activities of TS@PAP scaffolds have been characterized *in vitro*. As illustrated in supporting information, TS@PAP presented the acceptable impact on osteogenesis and osseointegration activities by comparing with TS and Control group (Fig. S3).

CCK-8 was used to assess the cell proliferation and cytotoxicity assays after co-cultivation with the drug-loaded 3D-printed titanium alloy implants for 24, 48, and 72 h. All the prostheses in the control, TS, and TS@PAP groups were co-cultured with five types of human osteosarcoma cells (143 B, MG63, HOS, U2OS, and SAOS2) in a culture environment with a pH of 6.5. Fig. 4B–F shows that TS and TS@PAP are not toxic to the cells, whereas TS@PAP exhibits a significant antitumor effect via the PTX released from the titanium alloy implant under acidic conditions. TS@PAP could reduce the cell activity to approximately 50%, which was significantly different from that observed in the TS group. After co-cultivation for 72 h, the cell activity of the five osteosarcoma cell lines decreased to less than 5% of the original value. For a more intuitive observation of the effect of PTX, 143 B osteosarcoma cells were selected to further observe the cell survival status using the live/dead staining technique. After co-cultivation with TS@PAP for 24 h, the living 143 B cell exhibited green fluorescence in the solution with a pH of 7.4, while a large number of dead cells exhibited red fluorescence in the solution with a pH of 6.5. As shown in Fig. 4A, living cells are scarce after co-cultivation for 72 h, indicating an inhibitory effect on osteosarcoma cell activity.

The five osteosarcoma cells were co-cultured with drug-loaded implants for apoptosis detection. After co-cultivation for 48 h, the cells in the control group were mostly alive, accounting for 77.68%–91.36% of the total cells. The TS@PAP group was dominated by late apoptotic cells, accounting for 20.31%–58.21% of the total cells. Consistent with this result, the late-stage apoptotic cells accounted for 24.31%–59.64% in the PTX drug-treated group (Fig. 5A). In all the osteosarcoma cell lines, the quantitative results of the apoptotic cells caused by TS@PAP implants and PTX were statistically significant ($P < 0.01$) compared with the control group (Fig. 5B–F). The quantitative results of the apoptotic cells caused by the drug-loaded implants and free PTX in the HOS, MG63, and SAOS2 cell lines were not statistically significant ($P > 0.05$). Similarly, these osteosarcoma cells were concentrated during late apoptosis in both TS@PAP and free PTX. Paclitaxel can reduce the activity of osteosarcoma cells, because it acts as a microtubule stabilizer, significantly affecting the stability of intracellular microtubule bundles by promoting tubulin polymerization, leading to spindles during cell mitosis [42,43]. Formation is hindered, causing cell cycle arrest and apoptosis [42,44]. Related studies on this mechanism have confirmed that this effect can occur in the treatment of osteosarcoma, breast cancer, ovarian cancer, and other tumors [45–47]. In this study, flow cytometry was used to detect the apoptosis of five types of osteosarcoma cells. The results showed that under the action of drug release from drug-loaded implants, these five osteosarcoma cells exhibited different degrees of apoptosis, with all of them being mainly late-stage apoptosis. This was consistent with the apoptosis of PTX alone as well as with the results of previous studies on the action mechanism of PTX [14,48].

2.6. *In vivo* effectiveness of drug-loaded 3D-printed titanium alloy implants

After the establishment of the osteosarcoma model, the nude mice were randomly divided into control, TS, TS&PTX, and TS@PAP groups. The prepared implants were inserted into the subcutaneous tissue adjacent to the tumor in the TS, TS@PAP, and TS&PTX groups (Fig. 6A). Paclitaxel was injected in the TS&PTX group through the tail vein, while the same amount of saline was injected in the control, TS, and TS@PAP groups. After implantation of the prosthesis, basic information related to the physiological state of each mouse was recorded, including the weight, skinfold thickness, tumor size, and survival time. The tumor volume in the TS and control groups was considerable at 28 d, and there was no evident difference between the two groups. Although the tumor volume in the TS&PTX group was significantly reduced, there were still evident

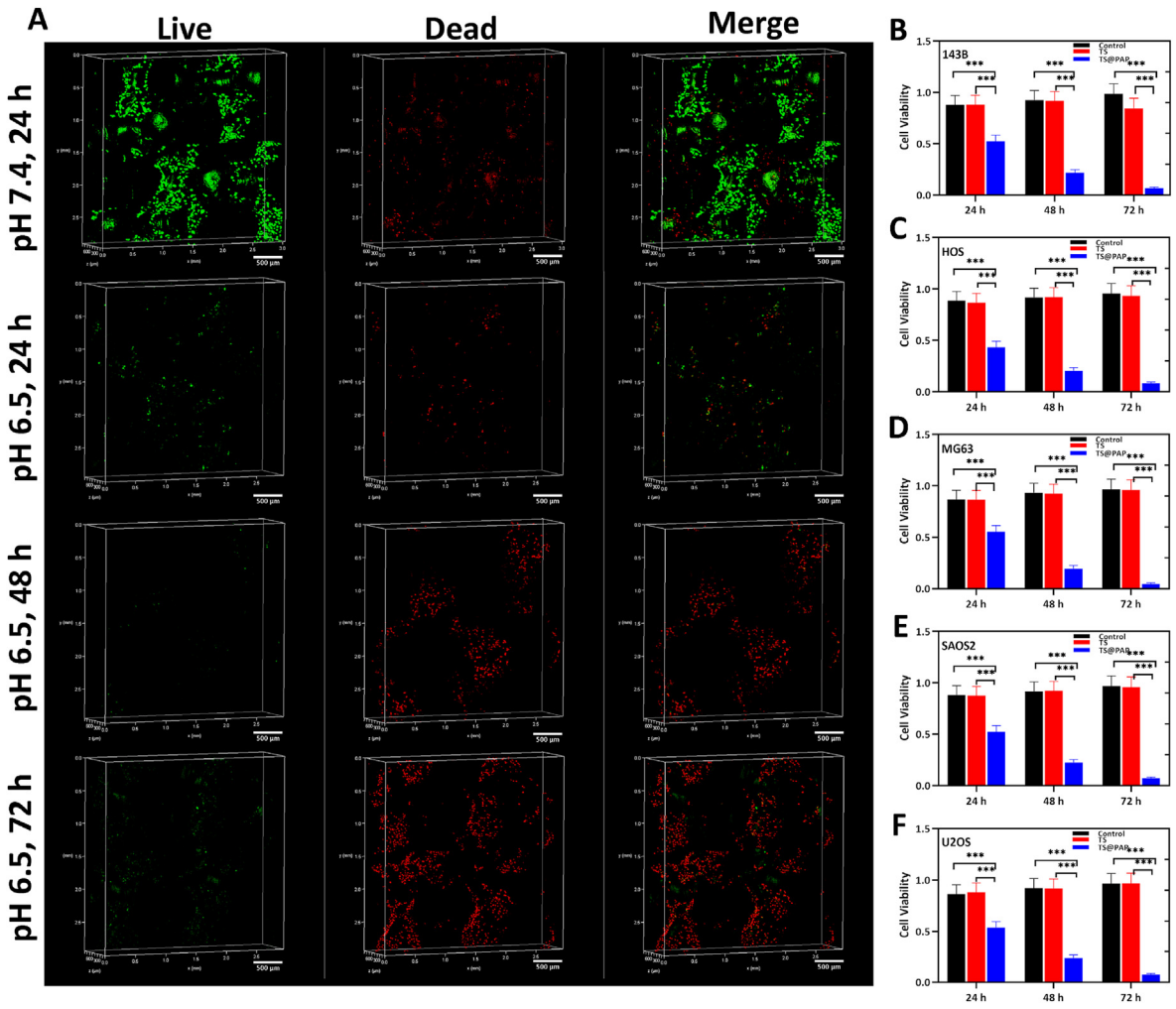

Fig. 4. (A) Live/dead staining of TS@PAP implants co-cultured with the 143 B osteosarcoma cell line, scale bar: 500 μm. (B–F) Cell viability of co-cultured 3D-printed titanium alloy implants with osteosarcoma cells in a solution with a pH of 6.5 ($n = 5$, $^{*}P < 0.05$, $^{***}P < 0.01$).

tumors. While the tumors in the TS@PAP group were significantly smaller than those in the TS and control groups, the tumors were almost invisible to the naked eye (Fig. 6B and C). X-ray imaging and tumor measurement of the four groups of mice confirmed that both the TS&PTX and TS@PAP groups could achieve a certain tumor suppression effect (Fig. 6D and E).

Combined with the comparative analysis of the tumor volume changes in the different groups, the tumor volume in the control and TS groups increased significantly; on day 28, the tumor volumes were 1683.94 ± 108.43 mm^3 and 1721.26 ± 105.34 mm^3, respectively, and the difference was not statistically significant ($P > 0.05$). In comparison, the increase in the tumor volume was less in the TS@PAP and TS&PTX groups, with values of 73.82 ± 57.4 mm^3 and 33.89 ± 24.5 mm^3 on day 28, respectively. Compared with the control group, the differences were statistically significant ($P < 0.01$) (Fig. 6F).

The mice in the TS@PAP group had the most significant increase in the body weight, from 14.31 ± 0.66 g to 19.21 ± 0.65 g, whereas the mice in the TS&PTX group had the most significant decrease, from 14.27 ± 0.59 g to 13.54 ± 0.58 g. There was no statistically significant difference between the TS and control groups ($P > 0.05$), and the weight difference between the TS@PAP and TS&PTX groups was statistically significant ($P < 0.01$) (Fig. 6G). In addition, the mice were systematically recorded and analyzed for the survival time; 62.5% (5/8) of the mice in the TS@PAP group were still alive on day 60 at the end of the observation. The longest survival time was 60 d in the TS@PAP group, with a median survival time of 59.25 d. The longest survival times of the mice in the control and TS groups were 29 and 30 d, respectively. The longest survival times of the mice in the TS&PTX and PTX groups were 38 and 37 d, respectively, with median survival times of 34.38 and 33.13 d (Fig. 6H). Figs. S4 and S5 showed the X-ray bone map images and a comparative analysis of the tumor volume in the different groups.

Among the five types of osteosarcoma cells, namely 143 B, HOS, MG63, SAOS2, and U2OS, the drug-loaded titanium alloy implants showed significant cell activity inhibition. To explore the tumor suppression effect *in vivo*, a subcutaneous model of the human-derived osteosarcoma was established in nude mice, simulating the process of local tumors with size ranging from small to large in the case of incomplete tumor resection and relapse [49,50]. The construction of the experimental model is consistent with the widely-established building schemes employed for subcutaneous tumor models, and the 143 B human osteosarcoma cell line was selected to evaluate the response of the model to the drug closer to the actual clinical situation [51,52]. In this experiment, a comparison between the drug-loaded implants and blank implants + systemic chemotherapy (PTX intravenous injection) was made. The comparison between the groups helped simulate the first-line clinical treatment plan, that is, surgical treatment + postoperative systemic chemotherapy [1,2]. The results showed that the systemic chemotherapy group experienced severe systemic side effects, particularly significant weight loss, which ultimately led to a certain level of tumor treatment, and the overall survival could not be effectively improved. The locally

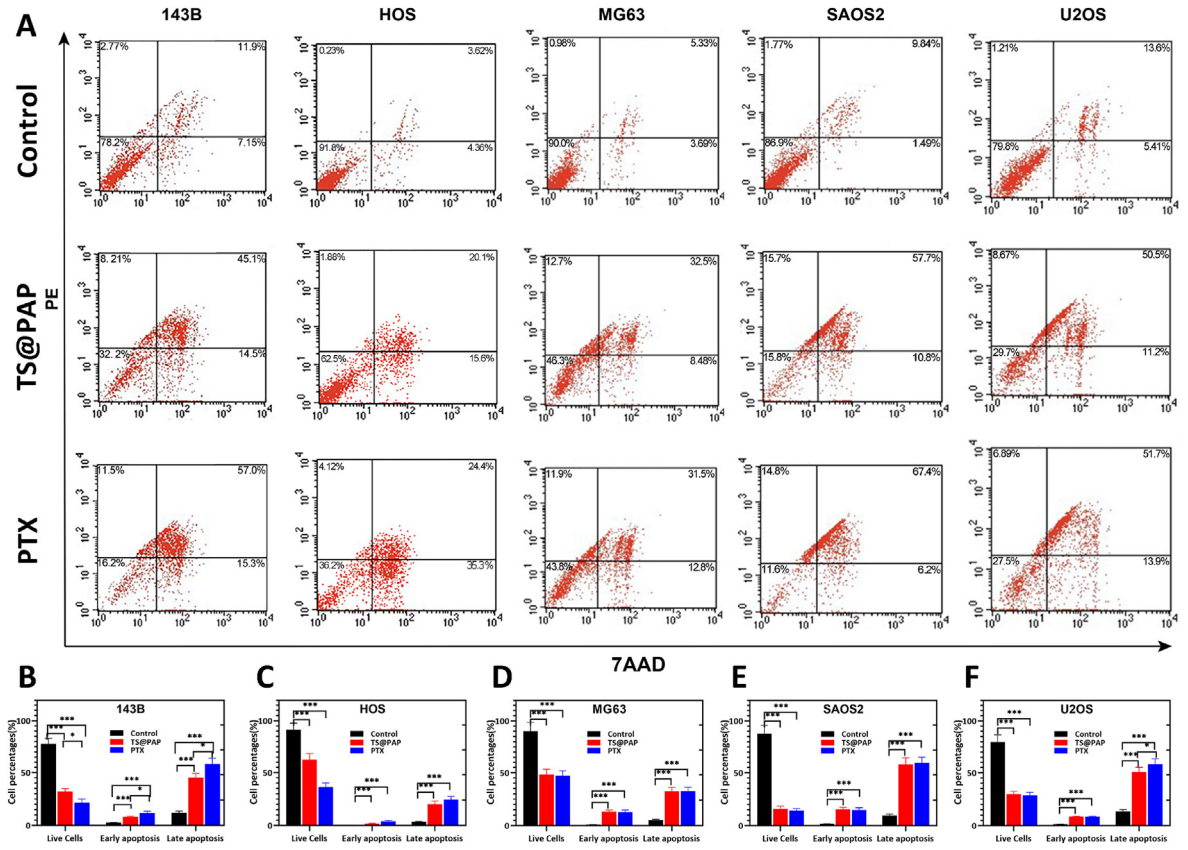

Fig. 5. (A) Apoptosis detection after co-cultivation of TS, TS@PAP or PTX with osteosarcoma cells in a solution with a pH of 6.5. (B–F) Quantitative analysis of apoptosis detection after co-cultivation with osteosarcoma cells for 48 h in a solution with a pH of 6.5 ($n = 5$, $^{*}P < 0.05$, $^{***}P < 0.01$).

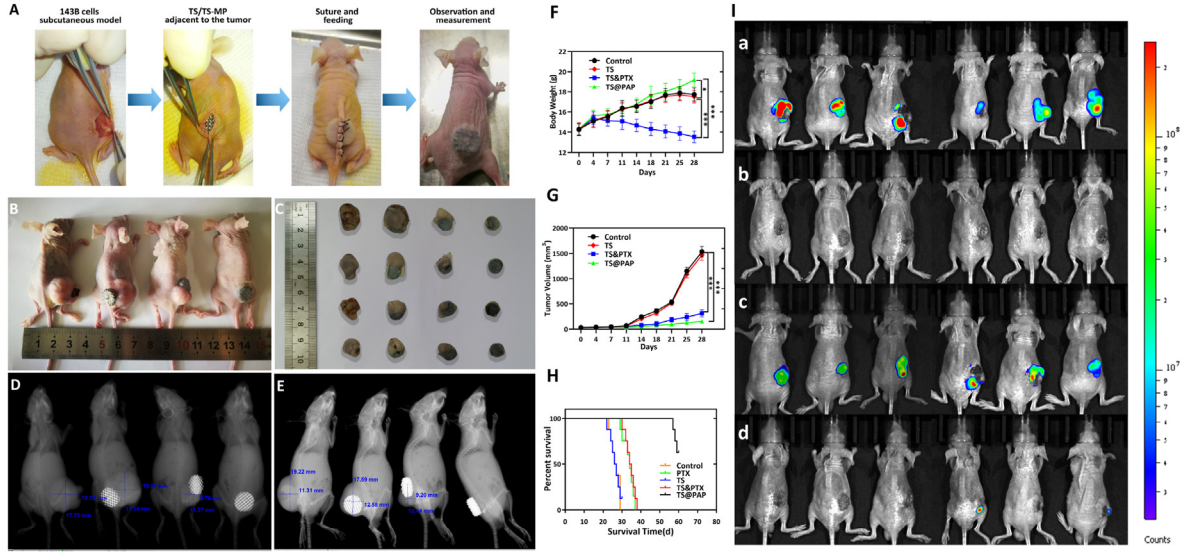

Fig. 6. (A) *In vivo* treatment of osteosarcoma in each group of mice. (B) Tumor *in vivo*. (C) Tumor *in vitro*. (D) X-ray orthoimaging and measurement of experimental mice. (E) X-ray lateral view film and measurement of the changes in the tumor size. Changes in the (F) body weight, (G) tumor size, and (H) survival curves of the mice in each group ($n = 6$, $^{*}P < 0.05$, $^{***}P < 0.01$). (I) *In vivo* anti-recurrence efficacy of the drug-loaded TS@PAP in the recurrent osteosarcoma model with Luc-labeled 143 B cells injected around the implant. (a) Third-day post cell injection, *in vivo* animal living fluorescence observation. (b) Tumor recurrence was fully controlled after another six days. (c) Following another cell injection, tumor recurrence was observed on day 12. (d) Tumor recurrence was partly controlled after another six days.

implanted drug-loaded 3D-printed titanium alloy implants had an advantage in local drug delivery. The drug directly affected the tumor localities to kill tumor cells, inhibit tumor growth, and prevent osteosarcoma recurrence. Therefore, based on the response to changes in the local pH during tumor growth, this study confirmed that drug-loaded 3D-printed titanium alloy implants are effective for systemic

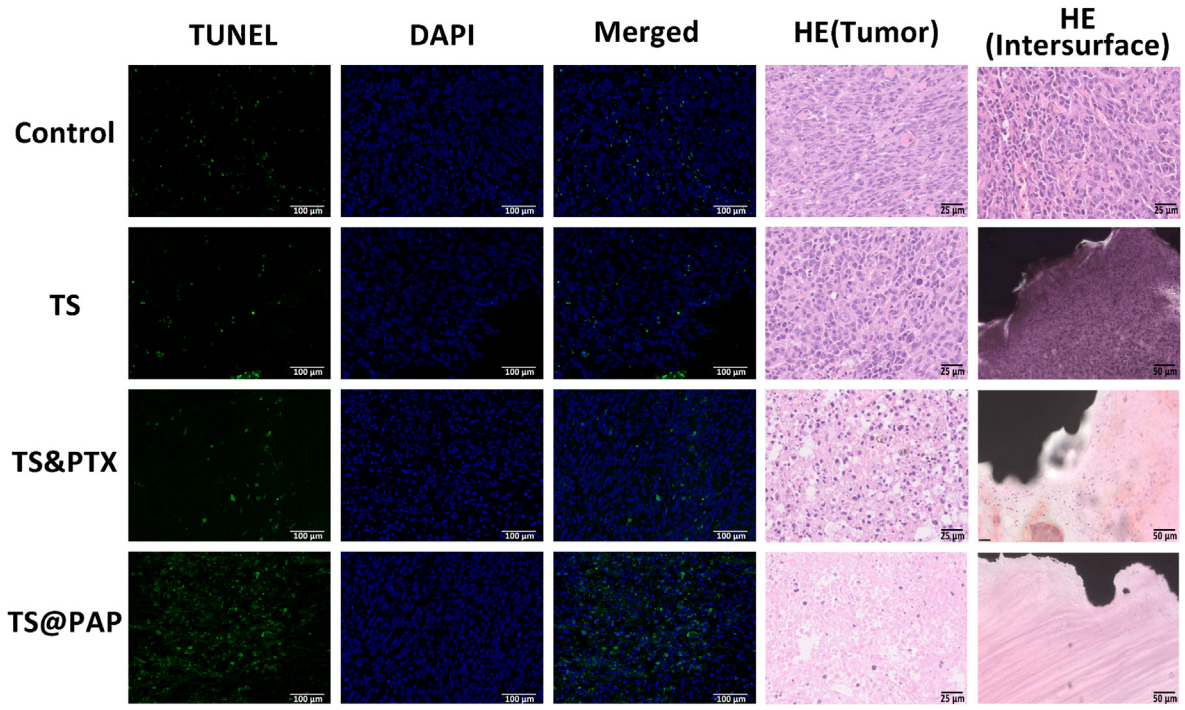

Fig. 7. TUNEL (scale bar: 100 μm) and HE (scale bar: 25 μm) staining images of tumor sections in each group. The scale bar in the HE staining images of TS-tumor interface sections represents 50 μm.

chemotherapy and can be applied to resolve the contradiction between local tumor control and normal tissue growth as a future direction for related research.

2.7. *In vivo* anti-recurrence efficacy of TS@PAP

Based on the above results, we hypothesized that drug-loaded TS@PAP could be sensitive to pH variations caused by osteosarcoma recurrence and PTX drug release. With the tumor recurrence models described above, TS@PAP implants were implanted subcutaneously in nude mice and sutured. Seven days after surgery, the incision healed well and the implant was surrounded by soft tissue. With 5×10^7 Luc-labeled 143 B cells injected around the implant, the mice were observed with an *in vivo* animal living fluorescence observer, as shown in Fig. 6I. On the third day after cell injection, the formation of a clear tumor recurrence state could be confirmed by the bioluminescence signals. Interestingly, the tumor recurrence was effectively controlled after another six days. To fully explore the limitation of the effect of TS@PAP on the treatment of tumor recurrence, Luc-labeled 143 B cells were again locally injected. Tumor recurrence was observed on day 12. After another six days, tumor recurrence was effectively controlled in most of the mice (4/6). Unfortunately, two mice had uncontrolled tumors at the time of observation. All these tumors continued to develop without being re-controlled during subsequent feedings of the mice. Overall, TS@PAP could eliminate at least one local tumor recurrence. In some cases, we believe two local tumor recurrences can be eliminated.

2.8. Histological analysis of the test samples of animal models

The analysis of the antitumor effectiveness is limited to the size of the tumor. Simply recording and analyzing body weight is insufficient. It is necessary to fully analyze the actual changes in the tumor. Therefore, a reasonable histological analysis is necessary. On day 28 of the experiment, nude mice were sacrificed, and their heart, liver, spleen, lungs, and kidneys were harvested. Hematoxylin and eosin (HE) staining revealed no evident organ injury in any group. Myocardial cells, hepatocytes, spleen cells, lung cells, glomerulus, and tubules were stained and washed without any evident abnormality (Fig. S6). A large number of deeply stained tumor cells were distributed in the control and TS groups, and there were many tumor cells distributed in the tumor body and at the interface with the TS implant. In the TS&PTX group, the number of deep-stained nuclear cells was reduced, and the distribution was sparser than that in the previous two groups. In the TS@PAP group, the deep-stained tumor cells inside the tumor were significantly reduced, and more fibrous tissues were generated in the tissue. Particularly when the tumor was exposed to TS@PAP at the implant interface, a large amount of fibrous tissues could be observed without evident tumor cells (Fig. 7).

During apoptosis, some endonucleases will cut the DNA between nucleosomes, and the broken DNA will expose 3′-OH. Terminal deoxynucleotidyl transferase (TdT) can achieve catalytic band fluorescence (FITC), while dUTP is combined with 3′-OH to achieve fluorescent labeling [53,54]. This technique can effectively detect apoptosis; therefore, in this study, in addition to the HE staining of tumors, TUNEL staining was performed. The most evident fluorescent label was observed in the tumor sections of the TS@PAP group. Compared with the control and TS groups, the drug-loaded 3D-printed titanium alloy implants showed a significantly more prominent tumor cell apoptosis phenomenon. Combined with the drug release of the drug-loaded implant and the verification of the action mechanism of PTX in the previous experiment, it was confirmed that the drug-loaded titanium alloy implant achieves tumor growth inhibition *in vivo*.

3. Conclusions

In summary, we fabricated an intelligent system mainly composed of a 3D-printed TS and pH-responsive PTX-loaded NPs; the system exhibited excellent mechanical support and biological performance for effective tumor inhibition and recurrence prevention following osteosarcoma surgery. When co-cultivating with drug-loaded materials, bone stem cells could maintain good activity under normal body fluid conditions, while human osteosarcoma cells could be efficiently eradicated in an acidic microenvironment, demonstrating the excellent antitumor effect. From a

novelty perspective, our drug-loaded implants could help treat post-operative tumor recurrence in a mice model of osteosarcoma. The novel 3D-printed titanium alloy implant exhibited the dual functions of tumor therapy and osteosarcoma recurrence prevention, showing great potential in curing bone tumors and providing a new research direction to cure tumor-related bone complex diseases.

4. Experimental section

Materials: Acrylic chloride, 2-hydroxyethyl vinyl ether, PPTS, PTX, polyethylene glycol (PEG-OH), succinic anhydride, dichloromethane (DCM), triethylamine (TEA), dopamine hydrochloride, paraformaldehyde (2%), and methanol were purchased from J&K Scientific Ltd. High-sugar Dulbecco's modified eagle medium (DMEM), 1640 medium, α-MEM medium, fetal bovine serum (FBS), hanks' balanced salt solution, pancreatin with EDTA (0.25%), and penicillin-Streptomycin double antibiotic were purchased from Thermo Fisher Scientific Ltd. The CCK-8 kit, cell live/dead staining kit, cell apoptosis kit, and cell cytoskeleton (F-actin) staining kit were purchased from Solarbio Life Science Ltd. Cell lines 143 B, Hos and MG63 were purchased from American type culture collection (ATCC). Cell lines Saos2 and U2OS were supplied by China Infrastructure of Cell Line Resources. All other reagents were purchased from Beijing Chemical Reagent Company and used without further purification.

Preparation of the titanium scaffold: 3D-printed macroporous Ti6Al4V scaffolds ($\varnothing = 10$ mm, $H = 5$ mm) were designed using computer assisted design software (Magics, Materialise, Belgium) and fabricated layer by layer using electron beam melting printing technology (Q10plus, GE, America). The porous architecture was designed based on a dodecahedron unit cell with a pore size of 640 μm, strut diameter of 400 μm, and porosity of 73% [55–57], which was beneficial for the in-growth of bone and blood vessels. All the specimens were subjected to air blasting and successively washed in acetone, alcohol, and deionized water (DIW) in an ultrasonic cleaner for 20 min each and dried at 60 °C overnight. For simplicity, the Ti6Al4V scaffold is denoted by TS.

Synthesis of PEG-COOH: PEG-OH ($M_n = 750$ g/mol, 3.75 g, 5 mmol) and TEA (0.7 mL, 5 mmol) were dissolved in 60 mL of freshly distilled CH_2Cl_2, and then succinic anhydride (0.8 g, 8 mmol) was added to the solution. After stirring at room temperature for 8 h, the mixture was washed with 2 M aqueous HCl, saturated aqueous NaCl, and DIW several times and dried over anhydrous $MgSO_4$. After evaporating the solvent, the residue was precipitated in cold ether thrice to afford the white solid of PEG-COOH. ^{1}H NMR ($CDCl_3$, 400 MHz, ppm): δ 2.59–2.63 (m, 4H), 3.38 (s, 3H), 4.21 (t, 2H).

Synthesis of modified PTX prodrug: PEG-COOH (2.65 g, 3 mmol), 2-hydroxyethyl vinyl ether (0.27 g, 3 mmol), 1-Ethyl-3-(3-dimethylaminopropyl) carbodiimide hydrochloride (0.7 g, 3.6 mmol), and 4-dimethylaminopyridine (68 mg, 0.6 mmol) were added to a 100 mL round-bottomed flask equipped with a magnetic stirring bar, followed by the addition of 50 mL of freshly distilled CH_2Cl_2 to fully dissolve all the solids. The solution was cooled to 0 °C for 30 min and allowed to reach room temperature, and then further stirred for another 24 h to complete the reaction. Subsequently, the solution was washed with 2 M aqueous HCl, saturated aqueous NaCl, and DIW thrice and dried over anhydrous $MgSO_4$. The final product was precipitated into ether several times to afford the white powder of PEG–vinyl ether derivative. Under a nitrogen atmosphere, PEG–vinyl derivative (0.92 g, 1 mmol) was added dropwise into a dry DCM solution of PTX (1.71 g, 2 mmol) and PPTS (51 mg, 0.2 mmol) at 0 °C. After stirring for 24 h at room temperature, the reaction was quenched by adding K_2CO_3. The mixture was filtered through a pad of celite, and the filtrate was evaporated to obtain the crude product, followed by precipitating in ether several times to obtain the PAP prodrug.

Preparation of PAP NPs and PAP-loaded TS: The nano-precipitation technique was employed to prepare the NPs. Typically, 5 mg of PAP was dissolved in 1 mL of ethanol and added to 4 mL of DIW under stirring through a syringe within 1 h. Subsequently, the solution was dialyzed against DIW for 24 h (MWCO 3500 Da), and the samples were freeze-dried and stored at room temperature for further experiments. For PTX immobilization, scaffolds were first soaked in 10 mL of a freshly prepared dopamine hydrochloride solution (2 mg/mL, a pH of 8.5) in 10 mmol/L Tris buffer for 24 h to form a PDA layer on the surfaces. Different solutions of PAP have been tested for the coating on TS scaffolds including 1 mmol/L, 3 mmol/L, 5 mmol/L and 6 mmol/L. Thereafter, the samples were oscillated in a mixed solution of PAP (5 mmol/L, pH 7.4) for 6 h, denoted by TS@PAP.

Characterizations of PAP NPs: TEM images were captured using a JEM-2200FS microscope (JEOL, Japan). A 5 μL droplet of the assembled solution was dropped onto a copper grid (300 mesh) coated with a carbon film, followed by drying at room temperature. The size distribution and zeta potentials of the PAP NPs were characterized by DLS using a Zetasizer (Nano-ZS, Malvern, UK) with a 632.8 nm laser light set at a scattering angle of 173°. Each measurement was performed in triplicate, and the results were processed with Zetasizer Software (version 7.02).

Microstructure and composition: To determine the changes in the TS surface and microstructure, SEM and EDS were performed [58]. All samples were first freeze-dried at 50 °C and 1.95 mbar for three days in a vacuum freeze drier (MD-230; Thermo Fischer, USA). Thereafter, SEM was used to determine the surface morphology. EDS was attached to the SEM apparatus and used to characterize the chemical composition.

Drug concentration and bioactivity observation: The PTX concentration was measured by HPLC on a Shimadzu LC-20AT system with UV detection at 227 nm. A mixture of acetonitrile and DIW at 1/1 (v/v) was used as the mobile phase at a flow rate of 1.0 mL/min. Fluorescence spectra were recorded on a Hitachi F4600 photoluminescent spectrometer with a xenon lamp as the light source. Confocal laser scanning microscopy (CLSM) images were obtained using a TCS SP8 microscope (Leica Germany).

In vitro drug release of TS@PAP: The release profile of PTX from TS@PAP was studied using a dialysis tube (MWCO 3500 Da) under shaking (100 rpm) at a temperature of 37 °C in a phosphate buffer with a pH of 7.4 and acetate buffer with a pH of 6.5. Typically, 2 mL of the NP solution was dialyzed against 30 mL of the release media. At predetermined intervals, 10 mL of the release medium was withdrawn and refilled with an equal volume of fresh medium. Subsequently, the concentration of PTX in the medium was determined by HPLC measurements. The cumulative release ratio of PTX was calculated using the following formula:

$$R_i = \begin{cases} \dfrac{V_0 C_i}{m_{drug}} \times 100\% & (i = 1) \\ \dfrac{V_0 C_i + V_e \sum_1^{i-1} C_{i-1}}{m_{drug}} \times 100\% & (i \geq 2) \end{cases}$$

Here, R_i is the cumulative release ratio of PTX (%), m_{drug} is the total mass of PTX in the NPs (μg), V_0 and V_e are the volumes of the total release medium and exchanged medium, respectively (mL), and C_i is the PTX concentration in the release medium withdrawn at the ith time (μg/mL).

Stability and pH-responsive degradation of PAP: The storage stability and pH-responsive degradation behavior of the NPs were investigated by determining their size distributions using DLS before and after treating in the pH solutions (pH values of 7.4 and 6.5) at room temperature. After incubation of 4 h, their morphology and size variation were characterized by TEM and DLS.

In vitro cytotoxicity and antitumor efficiency of TS@PAP: Bone marrow mesenchymal stem cells of sprague dawley rats were applied in the *in vitro* cytotoxicity evaluation of the TS@PAP group compared with the TS control group without drug loading. The cells were incubated at 37 °C in Gibco α-MEM medium (pH of 7.4) supplemented with 10% FBS in a 5% CO_2 incubator. The cells were seeded on the surface of TS and TS@PAP in 24-well plates at a seeding density of 5×10^4 cells/well. After culturing

for 12 h, the medium was replaced by 100 μL of fresh medium, and 10 μL of CCK-8 was added to each well, followed by incubation at 37 °C with 5% CO_2 for 3 h. The absorbance of the resulting solutions was measured using a micro-plate reader at 570 nm. The relative cell viability was determined by comparing the absorbance at 570 nm with that of the control wells with untreated cells. The same procedure was applied to the scaffold and cells with co-culture times of 48 and 72 h. The data are presented as average ± SD ($n = 5$). Another group of scaffolds was co-cultured with cells in the 24-well plate for 48 h. The cytoskeletal state was reflected with F-actin stained by kit TRITC Phalloidin. The CLSM images were stored with the cytoskeletal status of the cells on the surface of scaffolds. Osteoblast precursor cells (MC3T3-E1 cell lines) were cultured in leach liquor of TS scaffolds, TS@PAP scaffolds and 0.1 μmol/L of paclitaxel solution for 7 days. After differentiation, alkaline phosphatase staining and alizarin red staining were performed, while RUNX2 and ALP genes were detected by PCR in another test.

The *in vitro* anticancer activity of TS@PAP was evaluated using human osteosarcoma cells 143 B as the model cells. The cells were incubated at 37 °C in HyClone DMEM supplemented with 10% FBS in a 5% CO_2 incubator. The cells were seeded in 96-well plates at a seeding density of 5×10^3 cells/well. After 48 h, the medium was replaced by 100 μL of fresh medium, and 10 μL of CCK-8 was added to each well, followed by incubation at 37 °C with 5% CO_2 for 3 h. The absorbance of the resulted solutions was measured using a micro-plate reader at 570 nm. The relative cell viability was determined by comparing the absorbance at 570 nm with that of the control wells with untreated cells. The data are presented as average ± SD ($n = 5$).

In vivo antitumor efficiency: A total of 30 BABL/C nude mice were used as model animals with a body weight in the range of 10–12 g in the initial test. Osteosarcoma models were established with 1×10^6 143 B osteosarcoma cells mixed in 100 μL of PBS injected directly under the skin on the lower right side of the back of the nude mice. When the average volume of the tumor site reached approximately 100 mm^3, the tumor-bearing mice were divided into four groups (six mice/group) and treated with saline, TS, TS&PTX, and TS@PAP. For the TS&PTX group, 4 μg equivalent concentration of free PTX per gram of the mice body weight was injected every three days. For the control, TS, and TS@PAP groups, the same volume of saline was injected through the tail vein. The tumor size and body weight of the mice were measured every three days. The tumor volume was calculated using the formula: volume = (length × $width^2$)/2. All the surgical interventions and postoperative animal care procedures were approved by the Animal Research Committee of Peking University (LA2020465).

To further validate the therapeutic effects of TS@PAP, we established a tumor recurrence model by repeatedly injecting osteosarcoma cells subcutaneously in BALB/c nude mice. TS@PAP implants were implanted subcutaneously in the nude mice and sutured for the first-time treatment based on the same tumor model described above. Seven days post-surgery, the incision healed well and the implant was surrounded by soft tissue. To fully simulate the tumor local recurrence scenario, 5×10^7 Luc-labeled 143 B cells were injected around the implant. The mice were observed using an *in vivo* animal living fluorescence observer every three days after cell injection. Once the in-vivo fluorescence could not be effectively observed, we proceeded to the next osteosarcoma cell injection.

Immunohistochemistry and immunofluorescence: After treatments, the tumors and major organs, including the heart, liver, spleen, lungs, and kidneys, were harvested and fixed in 4% paraformaldehyde solution. Subsequently, all the tissues were dehydrated with ethanol at serial concentrations, transparentized with xylene, and embedded in paraffin. Paraffin sections (7 μm) were dewaxed, rehydrated, and incubated with 0.3% H_2O_2 in methanol. For HE staining, the tissue sections were stained with Mayer's hematoxylin for 3 min and eosin Y for 2 min and observed under a light microscope (Leica, Germany). For immunofluorescence, the tumor sections were incubated with protease K (10 μg/mL, a pH of 7.4) at 37 °C for 15 min. After being rinsed twice with PBS, the slices were incubated with a FITC-labeled TUNEL reaction reagent for 1 h at 37 °C in a humidified atmosphere in the dark. After being washed five times with PBS, the slices were stained with DAPI and examined using CLSM.

Credit author statement

Daoyang Fan and **Zhongjun Liu**: Conceptualization, Methodology. **Zhongjun Liu**, **Weifeng Liu**, and **Feng Wei**: Supervision. **Daoyang Fan**, **Chaoqi Zhang**, **Hufei Wang** and **Qingguang Wei**: Visualization, Methodology, Investigation, Data curation. **Hong Cai** and **Zhilei Bian**: Software, Validation. **Daoyang Fan**: Data curation, Writing- Original draft preparation. **Xing Wang** and **Zhongjun Liu**: Funding acquisition, Project administration, Supervision, Writing- Reviewing and Editing.

Ethics approval and consent to participate

Laboratory Animal Welfare Ethical Review Approval.

Approval number LA2020465.

The members of the Laboratory Animal Welfare Ethics Branch of the Biomedical Ethics Committee of Peking University reviewed the research plan of the project "Construction and Evaluation of Functionalized 3D Printed Titanium Alloy Implants" by Professor Liu Zhongjun of the Department of Orthopedics, Peking University Third Hospital, and believed that this plan was an animal experiment. In compliance with the ethical requirements of animal welfare, we agree to conduct experiments in accordance with this protocol.

Note: Animal experiments are carried out after obtaining the approval letter.

Declaration of competing interest

The authors declare no conflict of interest.

Data availability

Data will be made available on request.

Acknowledgements

This work was supported by grants from the National Natural Science Foundation of China (51973226, 82170211, 82172395, 32100698), Youth Innovation Promotion Association CAS (2019031), Ministry of Science and Technology of the People's Republic of China (2016YFB1101501, 2021YFC2400500), Beijing Natural Science Foundation (L212042, 7222318), Beijing Municipal Administration of Hospitals Incubating Program (PX2021015), and Beijing Jishuitan Hospital Elite Young Scholar Programme (XKGG202105). D. Fan was supported in part by the Henan postdoctoral research start-up project. We also received research and financial support from the Beijing AKEC Medical Co., Ltd.

Appendix A. Supplementary data

Supplementary data to this article can be found online at https://doi.org/10.1016/j.mtbio.2023.100683.

References

[1] J. Gill, R. Gorlick, Advancing therapy for osteosarcoma, Nat. Rev. Clin. Oncol. 18 (2021) 609–624.
[2] P.S. Meltzer, L.J. Helman, New horizons in the treatment of osteosarcoma, N. Engl. J. Med. 385 (2021) 2066–2076.
[3] C. Yang, Y. Tian, F. Zhao, Z. Chen, P. Su, Y. Li, A. Qian, Bone microenvironment and osteosarcoma metastasis, Int. J. Mol. Sci. 21 (2020) 6895.
[4] D.J. Harrison, D.S. Geller, J.D. Gill, V.O. Lewis, R. Gorlick, Current and future therapeutic approaches for osteosarcoma, Expet Rev. Anticancer Ther. 18 (2018) 39–50.
[5] N.F. Yasin, M.L. Abdul Rashid, V. Ajit Singh, Survival analysis of osteosarcoma patients: a 15-year experience, J. Orthop. Surg. 28 (2020) 1–11.

[6] T. Zhang, Q. Wei, H. Zhou, Z. Jing, X. Liu, Y. Zheng, H. Cai, F. Wei, L. Jiang, M. Yu, Y. Cheng, D. Fan, W. Zhou, X. Lin, H. Leng, J. Li, X. Li, C. Wang, Y. Tian, Z. Liu, Three-dimensional-printed individualized porous implants: a new "implant-bone" interface fusion concept for large bone defect treatment, Bioact. Mater. 6 (2020) 3659–3670.

[7] V.S. Goudar, M.P. Koduri, Y.N. Ta, Y. Chen, L.A. Chu, L.S. Lu, F.G. Tseng, Impact of a desmoplastic tumor microenvironment for colon cancer drug sensitivity: a study with 3D chimeric tumor spheroids, ACS Appl. Mater. Interfaces 13 (41) (2021) 48478–48491.

[8] H.J. An, H.S. Kim, J.A. Kwon, J. Song, I. Choi, Adjustable and versatile 3D tumor spheroid culture platform with interfacial elastomeric wells, ACS Appl. Mater. Interfaces 12 (6) (2020) 6924–6932.

[9] C. Zhu, M. He, D. Sun, Y. Huang, L. Huang, M. Du, J. Wang, J. Wang, Z. Li, B. Hu, Y. Song, Y. Li, G. Feng, L. Liu, L. Zhang, 3D-Printed multifunctional polyetheretherketone bone scaffold for multimodal treatment of osteosarcoma and osteomyelitis, ACS Appl. Mater. Interfaces 13 (40) (2021) 47327–47340.

[10] D. Fan, Y. Li, X. Wang, T. Zhu, Q. Wang, H. Cai, W. Li, Y. Tian, Z. Liu, Progressive 3D printing technology and its application in medical materials, Front. Pharmacol. 11 (2020) 122.

[11] H. Cai, Z. Liu, F. Wei, M. Yu, N. Xu, Z. Li, 3D printing in spine surgery, Adv. Exp. Med. Biol. 1093 (2018) 345–359.

[12] H. Wang, K. Su, L. Su, P. Liang, P. Ji, C. Wang, Comparison of 3D-printed porous tantalum and titanium scaffolds on osteointegration and osteogenesis, Mater. Sci. Eng. C 104 (2019), 109908.

[13] N. Xu, F. Wei, X. iu, L. Jiang, H. Cai, Z. Li, M. Yu, F. Wu, Z. Liu, Reconstruction of the upper cervical spine using a personalized 3D-printed vertebral body in an adolescent with ewing sarcoma, Spine 41 (2016) 50–54.

[14] S. Bonvalot, A. Gronchi, C. Le Péchoux, C.J. Swallow, D. Strauss, P. Meeus, F. van Coevorden, S. Stoldt, E. Stoeckle, P. Rutkowski, M. Rastrelli, C.P. Raut, D. Hompes, A. De Paoli, C. Sangalli, C. Honoré, P. Chung, A. Miah, J.Y. Blay, M. Fiore, J.J. Stelmes, A.P. Dei Tos, E.H. Baldini, S. Litière, S. Marreaud, H. Gelderblom, R.L. Haas, Preoperative radiotherapy plus surgery versus surgery alone for patients with primary retroperitoneal sarcoma (EORTC-62092: STRASS): a multicentre, open-label, randomised, phase 3 trial, Lancet Oncol. 21 (2020) 1366–1377.

[15] J.S. Whelan, L.E. Davis, Osteosarcoma, chondrosarcoma, and chordoma, J. Clin. Oncol. 36 (2018) 188–193.

[16] T.M. Abu Samaan, M. Samec, A. Liskova, P. Kubatka, D. Büsselberg, Paclitaxel's mechanistic and clinical effects on breast cancer, Biomolecules 9 (2019) 789.

[17] J. Xue, Z. Zhao, L. Zhang, L. Xue, S. Shen, Y. Wen, Z. Wei, L. Wang, L. Kong, H. Sun, Q. Ping, R. Mo, C. Zhang, Neutrophil-mediated anticancer drug delivery for suppression of postoperative malignant glioma recurrence, Nat. Nanotechnol. 12 (2017) 692–700.

[18] R.T. Shroff, M.M. Javle, L. Xiao, A.O. Kaseb, G.R. Varadhachary, R.A. Wolff, K.P.S. Raghav, M. Iwasaki, P. Masci, R.K. Ramanathan, D.H. Ahn, T.S. Bekaii-Saab, M.J. Borad, Gemcitabine, cisplatin, and nab-paclitaxel for the treatment of advanced biliary tract cancers: a phase 2 clinical Trial, JAMA Oncol. 5 (2019) 824–830.

[19] A.M. Sofias, M. Dunne, G. Storm, C. Allen, The battle of "nano" paclitaxel, Adv. Drug Deliv. Rev. 122 (2017) 20–30.

[20] Y. Zhang, K. Cai, C. Li, Q. Guo, Q. Chen, X. He, L. Liu, Y. Zhang, Y. Lu, X. Chen, T. Sun, Y. Huang, J. Cheng, C. Jiang, Macrophage-membrane-coated nanoparticles for tumor-targeted chemotherapy, Nano Lett. 18 (2018) 1908–1915.

[21] M. Vázquez-González, I. Willner, Aptamer-functionalized micro- and nanocarriers for controlled release, ACS Appl. Mater. Interfaces 13 (8) (2021) 9520–9541.

[22] J. Yan, T. Gao, Z. Lu, J. Yin, Y. Zhang, R. Pei, Aptamer-targeted photodynamic platforms for tumor therapy, ACS Appl. Mater. Interfaces 13 (24) (2021) 27749–27773.

[23] A. Nguyen, R. Böttger, S.D. Li, Recent trends in bioresponsive linker technologies of Prodrug-Based Self-Assembling nanomaterials, Biomaterials 275 (2021), 120955.

[24] W. Wang, J. Fan, G. Zhu, J. Wang, Y. Qian, H. Li, J. Ju, L. Shan, Targeted prodrug-based self-assembled nanoparticles for cancer therapy, Int. J. Nanomed. 15 (2020) 2921–2933.

[25] A. Xie, S. Hanif, J. Ouyang, Z. Tang, N. Kong, N.Y. Kim, B. Qi, D. Patel, B. Shi, W. Tao, Stimuli-responsive prodrug-based cancer nanomedicine, EBioMedicine 56 (2020), 102821.

[26] K.C. Corn, M.A. Windham, M. Rafat, Lipids in the tumor microenvironment: from cancer progression to treatment, Prog. Lipid Res. 80 (2020), 101055.

[27] E.C. Lien, A.M. Westermark, Y. Zhang, C. Yuan, Z. Li, A.N. Lau, K.M. Sapp, B.M. Wolpin, M.G. Vander Heiden, Low glycaemic diets alter lipid metabolism to influence tumour growth, Nature 599 (2021) 302–307.

[28] Y. Li, Q.N. Bui, L.T.M. Duy, H.Y. Yang, D.S. Lee, One-step preparation of pH-responsive polymeric nanogels as intelligent drug delivery systems for tumor therapy, Biomacromolecules 19 (2018) 2062–2070.

[29] S. Wang, G. Yu, Z. Wang, O. Jacobson, L.S. Lin, W. Yang, H. Deng, Z. He, Y. Liu, Z.Y. Chen, X. Chen, Enhanced antitumor efficacy by a cascade of reactive oxygen species generation and drug release, Angew. Chem. 58 (2019) 14758–14763.

[30] D. Huang, Y. Zhuang, H. Shen, F. Yang, X. Wang, D. Wu, Acetal-linked PEGylated paclitaxel prodrugs forming free-paclitaxel-loaded pH-responsive micelles with high drug loading capacity and improved drug delivery, Mater. Sci. Eng. C 82 (2018) 60–68.

[31] J. Yang, Q. Lv, W. Wei, Z. Yang, J. Dong, R. Zhang, Q. Kan, Z. He, Y. Xu, Bioresponsive albumin-conjugated paclitaxel prodrugs for cancer therapy, Drug Deliv. 25 (2018) 807–814.

[32] Y.X. Ye, S.Y. Wu, X.Y. Chen, Y.W. Yu, S.M. Zeng, Z.C. Wang, Q.C. Jiao, H.L. Zhu, Glutathione-responsive prodrug conjugates for image-guided combination in cancer therapy, Eur. J. Med. Chem. 225 (2021), 113746.

[33] Y. Sun, Y. Li, Y. Zhang, T. Wang, K. Lin, J. Liu, A polydopamine-assisted strontium-substituted apatite coating for titanium promotes osteogenesis and angiogenesis via FAK/MAPK and PI3K/AKT signaling pathways, Mater. Sci. Eng. C 131 (2021), 112482.

[34] C. Xu, Y. Xia, L. Wang, X. Nan, J. Hou, Y. Guo, K. Meng, J. Lian, Y. Zhang, F. Wu, B. Zhao, Polydopamine-assisted immobilization of silk fibroin and its derived peptide on chemically oxidized titanium to enhance biological activity in vitro, Int. J. Biol. Macromol. 185 (2021) 1022–1035.

[35] J. Hu, Q. Wang, N. Ma, B. Li, G. You, Y. Wang, Z. Chu, L. Zhao, H. Zhou, Characterization and biosafety evaluation of hemoglobin-based oxygen carriers coated with polydopamine, J. Biomed. Nanotechnol. 16 (2020) 1314–1323.

[36] P. Palladino, F. Bettazzi, S. Scarano, Polydopamine: surface coating, molecular imprinting, and electrochemistry-successful applications and future perspectives in analysis, Anal. Bioanal. Chem. 411 (2019) 4327–4338.

[37] B. Poinard, S. Kamaluddin, A.Q.Q. Tan, K.G. Neoh, J.C.Y. Kah, Polydopamine coating enhances mucopenetration and cell uptake of nanoparticles, ACS Appl. Mater. Interfaces 11 (2019) 4777–4789.

[38] S.J.L. Flatters, P.M. Dougherty, L.A. Colvin, Clinical and preclinical perspectives on Chemotherapy-Induced Peripheral Neuropathy (CIPN): a narrative review, Br. J. Anaesth. 119 (2017) 737–749.

[39] D. Słonina, D. Kabat, B. Biesaga, A. Janecka-Widła, W. Szatkowski, Chemopotentiating effects of low-dose fractionated radiation on cisplatin and paclitaxel in cervix cancer cell lines and normal fibroblasts from patients with cervix cancer, DNA Repair 103 (2021), 103113.

[40] B. Gantenbein-Ritter, C.M. Sprecher, S. Chan, S. Illien-Jünger, S. Grad, Confocal imaging protocols for live/dead staining in three-dimensional carriers, Methods Mol. Biol. 740 (2011) 127–140.

[41] Z. Duan, C. Chen, J. Qin, Q. Liu, Q. Wang, X. Xu, J. Wang, Cell-penetrating peptide conjugates to enhance the antitumor effect of paclitaxel on drug-resistant lung cancer, Drug Deliv. 24 (2017) 752–764.

[42] S.Y. Liu, S.X. Song, L. Lin, X. Liu, Molecular mechanism of cell apoptosis by paclitaxel and pirarubicin in a human osteosarcoma cell line, Chemotherapy 56 (2010) 101–107.

[43] R.M. Usman, F. Razzaq, A. Akbar, A.A. Farooqui, A. Iftikhar, A. Latif, H. Hassan, J. Zhao, J.S. Carew, S.T. Nawrocki, F. Anwer, Role and mechanism of autophagy-regulating factors in tumorigenesis and drug resistance, Asia Pac. J. Clin. Oncol. 17 (2021) 193–208.

[44] J.C. Leung, L. Cassimeris, Reorganization of paclitaxel-stabilized microtubule arrays at mitotic entry: roles of depolymerizing kinesins and severing proteins, Cancer Biol. Ther. 20 (2019) 1337–1347.

[45] M. Kavallaris, Microtubules and resistance to tubulin-binding agents, Nat. Rev. Cancer 10 (2019) 194–204.

[46] A. Müller-Deku, J.C.M. Meiring, K. Loy, Y. Kraus, C. Heise, R. Bingham, K.I. Jansen, X. Qu, F. Bartolini, L.C. Kapitein, A. Akhmanova, J. Ahlfeld, D. Trauner, O. Thorn-Seshold, Photoswitchable paclitaxel-based microtubule stabilisers allow optical control over the microtubule cytoskeleton, Nat. Commun. 11 (2020) 4640.

[47] X. Shi, X. Sun, Regulation of paclitaxel activity by microtubule-associated proteins in cancer chemotherapy, Cancer Chemother. Pharmacol. 80 (2017) 909–917.

[48] J. Riestra-Ayora, C. Sánchez-Rodríguez, R. Palao-Suay, J. Yanes-Díaz, A. Martín-Hita, M.R. Aguilar, R. Sanz-Fernández, Paclitaxel-loaded polymeric nanoparticles based on α-tocopheryl succinate for the treatment of head and neck squamous cell carcinoma: in vivo murine model, Drug Deliv. 28 (2021) 1376–1388.

[49] C. Blattmann, M. Thiemann, A. Stenzinger, E.K. Roth, A. Dittmar, H. Witt, B. Lehner, E. Renker, M. Jugold, V. Eichwald, W. Weichert, P.E. Huber, A.E. Kulozik, Establishment of a patient-derived orthotopic osteosarcoma mouse model, J. Transl. Med. 13 (2015) 136.

[50] M.V. Guijarro, S.C. Ghivizzani, C.P. Gibbs, Animal models in osteosarcoma, Front. Oncol. 4 (2014) 189.

[51] L.C. Sayles, M.R. Breese, A.L. Koehne, S.G. Leung, A.G. Lee, H.Y. Liu, A. Spillinger, A.T. Shah, B. Tanasa, K. Straessler, F.K. Hazard, S.L. Spunt, N. Marina, G.E. Kim, S.J. Cho, R.S. Avedian, D.G. Mohler, M.O. Kim, S.G. DuBois, D.S. Hawkins, E.A. Sweet-Cordero, Genome-informed targeted therapy for osteosarcoma, Cancer Discov. 9 (2019) 46–63.

[52] N.F. Wu, J. Yamamoto, M. Bouvet, R.M. Hoffman, A novel procedure for orthotopic tibia implantation for establishment of a more clinical osteosarcoma PDOX mouse model, In Vivo 35 (2021) 105–109.

[53] A.E. Kabakov, V.L. Gabai, Cell death and survival assays, Methods Mol. Biol. 1709 (2018) 107–127.

[54] R. Mirzayans, D. Murray, Do tunel and other apoptosis assays detect cell death in preclinical studies? Int. J. Mol. Sci. 21 (2020) 9090.

[55] X. Pei, L. Wu, C. Zhou, H. Fan, M. Gou, Z. Li, B. Zhang, H. Lei, H. Sun, J. Liang, Q. Jiang, Y. Fan, X. Zhang, 3D printed titanium scaffolds with homogeneous diamond-like structures mimicking that of the osteocyte microenvironment and its bone regeneration study, Biofabrication 13 (2020), 015008.

[56] T. Zhang, Q. Wei, D. Fan, X. Liu, W. Li, C. Song, Y. Tian, H. Cai, Y. Zheng, Z. Liu, Improved osseointegration with rhBMP-2 intraoperatively loaded in a specifically designed 3D-printed porous Ti6Al4V vertebral implant, Biomater. Sci. 8 (2020) 1279–1289.

[57] Y. Zhang, N. Sun, M. Zhu, Q. Qiu, P. Zhao, C. Zheng, Q. Bai, Q. Zeng, T. Lu, The contribution of pore size and porosity of 3D printed porous titanium scaffolds to osteogenesis, Mater. Sci. Eng. C 7 (2022), 112651.

[58] S. Sahab Negah, P. Oliazadeh, A. Jahanbazi Jahan-Abad, A. Eshaghabadi, F. Samini, S. Ghasemi, A. Asghari, A. Gorji, Transplantation of human meningioma stem cells loaded on a self-assembling peptide nanoscaffold containing IKVAV improves traumatic brain injury in rats, Acta Biomater. 92 (2019) 132–144.